

# Simulation Study on Nonlocal Transport for Peripheral Density Source<sup>\*</sup>)

Masatoshi YAGI, Naoaki MIYATO, Akinobu MATSUYAMA and Tomonori TAKIZUKA<sup>1)</sup>

*Japan Atomic Energy Agency, 2-166 Omotedate, Obuchi, Rokkasho, Aomori 039-3212, Japan*

<sup>1)</sup>*Graduate School of Engineering, Osaka University, 2-1 Yamadaoka, Suita, Osaka 565-0871, Japan*

(Received 10 December 2013 / Accepted 24 February 2014)

The simulation study of nonlocal transport for peripheral density source is performed using the 4-field reduced MHD model. A spherical density source is applied in the plasma edge, after saturation of the resistive ballooning turbulence is attained. After a while, the source is switched off. It is found that the nonlocal transport appears at the location far from the edge source, which induces not only (0,0) and ( $\pm 1, 0$ ) modes but also finite  $n$  modes, where ( $m, n$ ) indicates the set of poloidal mode number  $m$  and the toroidal mode number  $n$ . These modes interact with each other by the nonlinear and/or toroidal couplings. After switching-on the source, the formation of the spiral structure with poloidal rotation is observed, which yields a connection between core and edge regions. The simulation result indicates that 2D transport plays an essential role to the transient plasma response.

© 2014 The Japan Society of Plasma Science and Nuclear Fusion Research

Keywords: nonlocal transport, transient plasma response, toroidal coupling, edge and core coupling

DOI: 10.1585/pfr.9.3403030

## 1. Introduction

The transient transport events are observed in the magnetic confinement devices [1–9]. For example, the cold pulse experiment shows that a rapid transient increase in the electron temperature in the plasma core in response to an abrupt cooling of the edge. The time scale of the transient events is much faster than the diffusive time scale and the local transport model fails to reproduce them. The nonlocal transport was theoretically investigated based on the 1D integral heat flux model [10, 11]. The avalanche was considered as a candidate to explain the nonlocal transport [12, 13]. Inagaki et al. discussed the electron temperature fluctuations with a long radial correlation length in ECRH plasma of LHD [14]. It is speculated that such a long-range fluctuation plays a role for the fast pulse propagation. Recently, we have reported that the nonlocal transport appears when a toroidally-elongated cylindrical density source is applied at the plasma edge by 4-field Reduced MHD simulation [15]. It appears as a transient plasma response after switching-off the source. It is found that (1,0) mode plays a role to produce the nonlocal transport which is directly excited by the edge source. The essential difference with geodesic acoustic mode (GAM) is that externally applied density source excites it, not Reynolds stress by turbulence [16, 17]. It is confirmed that nonlocal transport does not appear in the cylinder limit, therefore, the toroidal coupling is essential like GAM.

In this work, simulation study of nonlocal transport in tokamak plasmas has been performed using the 4-field re-

duced MHD model. A spherical density source is applied in the plasma edge, after the steady state of resistive ballooning turbulence is attained. After a while, the source is switched off. To investigate the geometrical effect of source shape, it is compared with the toroidally-elongated cylindrical density source. It is found that the mechanism to produce the nonlocal transport is the same, however, it appears after switching-on the source for the spherical source, on the other hand, it appears just after switching-off it for cylindrical one. This paper is organized as follows. In section 2, the model equation is briefly explained and simulation results are discussed in section 3. The summary is given in section 4.

## 2. Model Equation

The 4-field reduced MHD model consists of vorticity equation, Ohm's law, parallel momentum equation, and density evolution equation [18, 19]. The poloidal Alfvén time and the plasma minor radius are used for the normalization. In the circular tokamak geometry ( $r, \theta, \zeta$ ), these are given by

$$\frac{dU}{dt} = -\nabla_{\parallel} J - [2r \cos \theta, p] + \mu \nabla_{\perp}^2 U, \quad (1)$$

$$\frac{\partial A}{\partial t} = -\nabla_{\parallel} F + \eta_{\parallel} J, \quad (2)$$

$$\frac{dv}{dt} = -\nabla_{\parallel} p + \mu_{\nu} \nabla_{\perp}^2 v, \quad (3)$$

$$\begin{aligned} \frac{dp}{dt} = & \hat{\beta}[r \cos \theta, F] - \hat{\beta} \nabla_{\parallel} (v + \delta J) \\ & + \kappa_{\perp} \nabla_{\perp}^2 p + \kappa_{\parallel} \nabla_{\parallel}^2 p + S, \end{aligned} \quad (4)$$

author's e-mail: yagi.masatoshi@jaea.go.jp

<sup>\*</sup>) This article is based on the presentation at the 23rd International Toki Conference (ITC23).

where  $d/dt = \partial/\partial t + [\phi, \cdot]$ ,  $\nabla_{\parallel} = \nabla_{\parallel}^{(0)} - [A, \cdot]$ ,  $[f, g] = (\partial f/\partial r)(\partial g/r\partial\theta) - (\partial f/r\partial\theta)(\partial g/\partial r)$ ,  $\nabla_{\perp}^2 = (\partial/r\partial r)(r\partial/\partial r) + \partial^2/r^2\partial\theta^2$ ,  $U = \nabla_{\perp}^2(\phi + \delta_i p)$ ,  $F = \phi - \delta_e p$ ,  $J = \nabla_{\perp}^2 A$ ,  $\tau = T_e/T_i$ ,  $\delta = c/(a\omega_{pi})$ ,  $\delta_i = \delta/(1 + \tau)$ ,  $\delta_e = \delta\tau/(1 + \tau)$ ,  $\hat{\beta} = \beta/(1 + \beta)$ .  $\delta$  is the normalized ion skin depth, which represents the finite Lamor radius effect. The magnetic curvature term is retained in Eqs. (1) and (4) to represent ballooning mode. The electron temperature is assumed to be isothermal, so that the pressure perturbation is determined only by the density perturbation. In this study, the spherical source is introduced in Eq. (4), which is given by

$$S = S_{AMP} \exp\left(-\frac{r^2 + r_s^2 - 2rr_s \cos\theta + \zeta^2/\epsilon^2}{2\Delta^2}\right), \quad (5)$$

where  $r_s$  represents the location of source,  $\epsilon$  is the inverse aspect ratio and  $\Delta$ , the half width of source, respectively. In the code, the finite difference in  $r$ , and pseudo-spectral in  $\theta$  and  $\zeta$  are adopted. The time step is advanced by the predictor-corrector method. The simulation parameters are chosen as  $\beta = 10^{-2}$ ,  $\delta = 10^{-2}$ ,  $\tau = 1$ ,  $\epsilon = 1/3$ ,  $\mu = 6.5 \times 10^{-6}$ ,  $\mu_v = 2.6 \times 10^{-5}$ ,  $\eta_{\parallel} = 10^{-5}$ ,  $\kappa_{\perp} = 2 \times 10^{-7}$ ,  $\kappa_{\parallel} = 1$ ,  $S_{AMP} = 10^{-2}$ ,  $r_s = 0.8$ ,  $\Delta = 0.1$ . The mesh size and the time step are given by  $257 \times 200 \times 100$  for  $(r, \theta, \zeta)$  and  $\Delta t = 10^{-3}$ , respectively. 2/3 de-aliasing rule is applied for the calculation of nonlinear terms. The initial equilibrium pressure is given by  $P_{eq}(r) = (\beta/\epsilon)(1 - r^2)^2$ . The initial current profile is calculated by the cylindrical force balance.

### 3. Simulation Result

In this simulation, the spherical source is applied at  $t = 960$  after saturation of the resistive ballooning turbulence, which is excited in the peripheral region. Then, the source is switched off at  $t = 1800$ . Figure 1 shows the time evolution of internal energy for each Fourier mode, which is defined by

$$E_{m,n} \equiv \frac{1}{2} \int_0^1 r dr |p_{m,n}(r)|^2, \quad (6)$$

where  $m$  and  $n$  represent the poloidal and toroidal mode numbers. The discrete Fourier transform (DFT) is given by

$$p_{m,n}(r) = \frac{1}{MN} \sum_{m=0}^M \sum_{n=0}^N p(r, \theta, z) \exp(im\theta + in\zeta). \quad (7)$$

It is shown that the energy is directly transferred into  $(0, 0)$  and  $(\pm 1, 0)$  modes as well as finite  $n$  modes from the source at  $t = 960$ . Figure 2 shows the time evolution of flux-averaged total density profile at  $t = 960, 1800, 2500$ , which is calculated by

$$P_{tot}(r) = P_{eq}(r) + p_{0,0}(r). \quad (8)$$

It is shown that the nonlocal transport appears after switching-on the source, namely, at  $t = 1800$ , which is different from the case with toroidally-elongated cylindrical

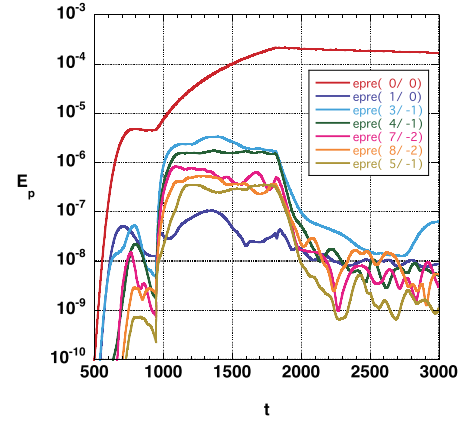


Fig. 1 Time evolution of internal energy for each Fourier mode.

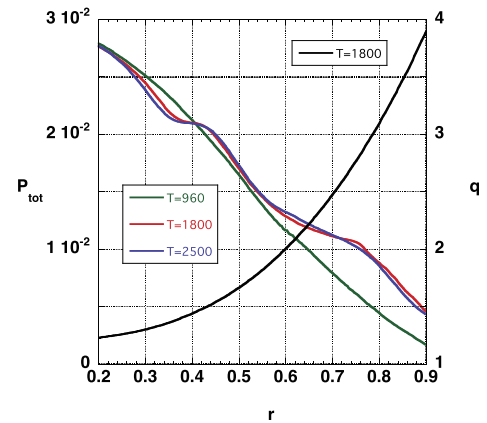


Fig. 2 Time evolution of flux-averaged total density profile and  $q$ -profile at  $t = 1800$ .

source ( $\zeta^2/\epsilon^2 \rightarrow 0$  in Eq. (5)). In that case, it appears just after switching-off the source. The essential difference between these sources is that the spherical source consists of not only  $(0, 0)$  and  $(\pm 1, 0)$  modes but also finite  $n$  modes. The  $q$ -profile is also shown in Fig. 2, where  $q$  indicates the safety factor. Although the nonlocal transport appears in the vicinity of  $q = 3/2$  surface, it is not an exact location of  $q = 3/2$  surface. Figure 3 shows the contour plots of density fluctuation in the poloidal cross section with  $\zeta = 0$  at  $t = 960$  (top) and  $t = 1800$  (bottom), which consist of only  $(\pm 1, 0)$  Fourier mode. The dipole structure starts to deform after the switching-on the source and the spiral structure appears, which connects the core region and edge region.

The detail analysis is carried out based on the energy balance equations for  $p_{0,0}(r)$ ,  $p_{\pm 1,0}(r)$  and  $v_{\pm 1,0}(r)$ , which are given by

$$\begin{aligned} \frac{\partial}{\partial t} \frac{1}{2} |p_{0,0}(r)|^2 &= p_{0,0}(r) N L_{0,0}^p(r) \\ &+ i \frac{\hat{\beta}}{2} p_{0,0}(r) (-k_{\theta} F_{-1,0}(r) + k_{\theta} F_{1,0}(r)) \\ &- i \frac{\hat{\beta}}{2} p_{0,0}(r) \left( \frac{\partial F_{-1,0}(r)}{\partial r} - \frac{\partial F_{1,0}(r)}{\partial r} \right) \\ &+ \kappa_{\perp} p_{0,0}(r) \nabla_{\perp}^2 p_{0,0}(r) + p_{0,0}(r) S_{0,0}, \end{aligned} \quad (9)$$

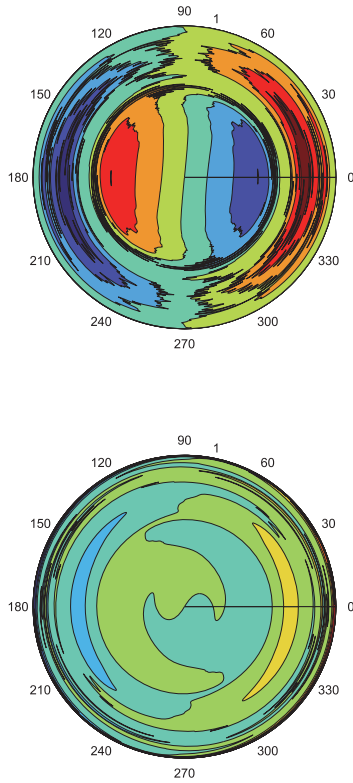


Fig. 3 Contour plot of density fluctuation in the poloidal cross section  $\zeta = 0$  at  $t = 960$  (top) and  $t = 1800$  (bottom), respectively. It consists of only  $(\pm 1, 0)$  Fourier mode.

$$\begin{aligned}
 \frac{\partial}{\partial t} \frac{1}{2} |p_{1,0}(r)|^2 &= \underbrace{p_{1,0}^*(r) NL_{1,0}^p(r)}_{\text{PRHS1}} \\
 &+ \underbrace{i \frac{\hat{\beta}}{2} p_{1,0}^*(r) (2k_\theta F_{2,0}(r))}_{\text{PRHS2}} \\
 &- \underbrace{i \frac{\hat{\beta}}{2} p_{1,0}^*(r) \left( \frac{\partial F_{0,0}(r)}{\partial r} - \frac{\partial F_{2,0}(r)}{\partial r} \right)}_{\text{PRHS2}} \\
 &- \underbrace{i \hat{\beta} \delta p_{1,0}^*(r) k_\parallel J_{1,0}(r)}_{\text{PRHS3}} - \underbrace{i \hat{\beta} p_{1,0}^*(r) k_\parallel v_{1,0}(r)}_{\text{PRHS4}} \\
 &+ \underbrace{\kappa_\perp p_{1,0}^*(r) \nabla_\perp^2 p_{1,0}(r)}_{\text{PRHS5}} + \underbrace{i p_{1,0}^* \frac{dP_{\text{eq}}}{dr} k_\theta \phi_{1,0}(r)}_{\text{PRHS6}} \\
 &- \underbrace{\kappa_\parallel p_{1,0}^* k_\parallel^2 p_{1,0} + p_{1,0}^*(r) S_{1,0}}_{\text{PRHS7}}, \quad (10)
 \end{aligned}$$

$$\begin{aligned}
 \frac{\partial}{\partial t} |v_{1,0}(r)|^2 &= \underbrace{v_{1,0}^*(r) NL_{1,0}^v(r)}_{\text{VRHS1}} \\
 &- \underbrace{i v_{1,0}^*(r) k_\parallel p_{1,0}(r)}_{\text{VRHS2}} - \underbrace{i \frac{dP_{\text{eq}}}{dr} v_{1,0}^*(r) k_\theta A_{1,0}(r)}_{\text{VRHS3}} \\
 &+ \underbrace{\mu_\nu v_{1,0}^*(r) \nabla_\perp^2 v_{1,0}(r)}_{\text{VRHS5}}. \quad (11)
 \end{aligned}$$

Here \* indicates the complex conjugate,  $p_{1,0}^*(r) = p_{-1,0}(r)$ ,

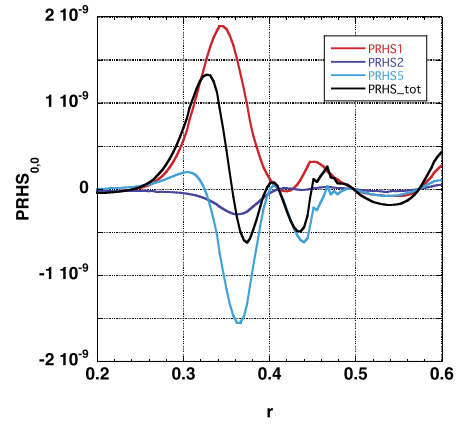


Fig. 4 Radial profile of each term in RHS of Eq. (9) at  $t = 1800$ .

$v_{1,0}^*(r) = v_{-1,0}(r)$  and  $k_\theta = m/r$ ,  $k_\parallel = mq(r) + n$  with  $m = 1$  and  $n = 0$  are wave numbers for  $(1, 0)$  mode. In Eq. (10), PRHS1 indicates the convective nonlinearity, PRHS2, the toroidal coupling, PRHS3, the compressibility by the current, PRHS4, the compressibility by the parallel ion velocity, PRHS5, the dissipation, PRHS6, the diamagnetic contribution of convective nonlinearity, PRHS7, the parallel thermal transport, respectively. In Eq. (11), VRHS1 indicates the convective nonlinearity, VRHS2, the compressibility by the density, PRHS3, the compressibility by the electromagnetic perturbation, PRHS5, the dissipation, respectively.

The convective nonlinearities are expressed by the three wave coupling as

$$\begin{aligned}
 NL_{m,n}^p(r) &= \sum_{\substack{m'+m''=m \\ n'+n''=n}} \left\{ -[\phi_{m',n'}(r), p_{m'',n''}(r)] \right. \\
 &\left. + \hat{\beta} [A_{m',n'}(r), v_{m'',n''}(r) + \delta J_{m'',n''}(r)] \right\}, \quad (12)
 \end{aligned}$$

$$\begin{aligned}
 NL_{m,n}^v(r) &= \sum_{\substack{m'+m''=m \\ n'+n''=n}} \left\{ -[\phi_{m',n'}(r), v_{m'',n''}(r)] \right. \\
 &\left. + [A_{m',n'}(r), p_{m'',n''}(r)] \right\}. \quad (13)
 \end{aligned}$$

Figures 4-6 show the radial profile of each term in RHS of Eqs. (9), (10) and (11) at  $t = 1800$ .

It is confirmed that the convective nonlinearity in Eq. (9) contributes the nonlocal transport, via three wave coupling  $(1, 0) + (-1, 0) \rightarrow (0, 0)$  comparing to the case without the convective nonlinearity in Eq. (9) after  $t = 960$ . On the other hand, the balance between the toroidal coupling (PRHS2) and the compressibility by the parallel ion velocity (PRHS4) in Eq. (10) mainly drives  $p_{\pm 1,0}$  modes (Fig. 4). Similarly,  $v_{\pm 1,0}$  mode is driven by the balance between the convective nonlinearity (VRHS1) and the compressibility by the electromagnetic perturbation (VRHS3) (Fig. 5). To confirm the importance of the toroidal coupling, the simulation in which the toroidal coupling is switched off at  $t = 960$  (in the cylinder limit) is also carried out. It is found that the nonlocal transport does not appear in this case [16, 17].

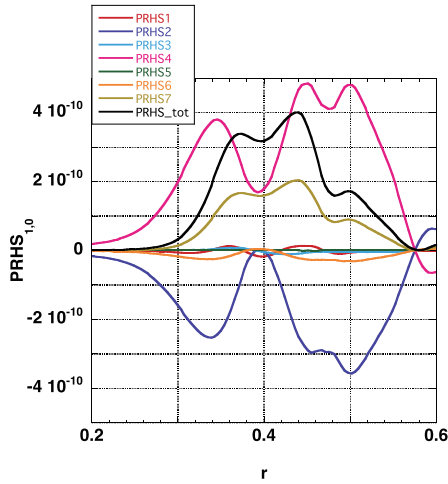


Fig. 5 Radial profile of each term in RHS of Eq. (10) at  $t = 1800$ .

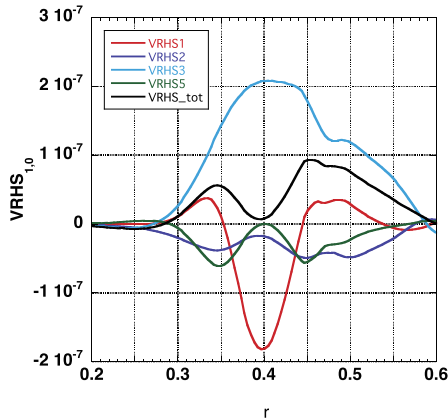


Fig. 6 Radial profile of each term in RHS of Eq. (11) at  $t = 1800$ .

## 4. Summary

The nonlinear simulation is performed using the 4-field RMHD model with density source to investigate the nonlocal transport phenomena. It is found that the nonlocal transport appears in the vicinity of  $q = 3/2$  surface after switching-on the source as a transient plasma response. In this simulation,  $p_{\pm 1,0}(r)$  modes play an important role in the nonlocal transport. The simulation result is summarized as follows: (1) When the spherical source is applied in the plasma edge, the energy is directly transferred into  $p_{0,0}(r)$  and  $p_{\pm 1,0}(r)$  modes as well as finite  $n$  modes (Fig. 1). (2) When the source is switched on, the dipole structure starts to deform and the spiral structure is formed by  $p_{\pm 1,0}(r)$  modes, which connects the core and the edge regions (Fig. 3). (3)  $p_{\pm 1,0}(r)$  modes interact with  $p_{0,0}(r)$  via the three wave coupling and the toroidal coupling, which produces the nonlocal transport in the vicinity of  $q = 3/2$  surface, which corresponds to the least rational number in this system. We confirm this mechanism not only by simulations without the convective nonlinearity in  $p_{0,0}(r)$

evolution equation or without the toroidal coupling (in the cylinder limit), but also by the detail analysis on each energy balance equation. It is found that the mechanism to produce the nonlocal transport is the same as the cylindrical source, however, it just appears after applying the source. The nonlocal transport obtained in this simulation is driven by the macroscopic structure, which shows some similarity to experimental observation [14]. Since the conventional 1D model can not reproduce such a macroscopic structure [10, 11], 3D treatment is necessary to understand the nonlocal transport. Introducing sink instead of source in peripheral region, we have preliminary investigated nonlocal transport, so far we did not find nonlocal transport in 4-field model. As future works, (1) the  $q$ -dependence (the role of rational surface), (2) the cold pulse propagation taking electron temperature fluctuation into account should be investigated to identify the nonlocal transport.

This work is partially supported by Grant-in-Aid for Scientific Research (No. 23246163). The simulations are performed by using HELIOS super computer in IFERC-CSC, Aomori, Japan.

- [1] L. Laurent, *Plasma Phys. Control. Fusion* **28**, 85 (1986).
- [2] E.D. Fredrickson, K. McGuire, A. Cavallo *et al.*, *Phys. Rev. Lett.* **65**, 2869 (1990).
- [3] L. Giannone, V. Erckmann, U. Gasparino *et al.*, *Nucl. Fusion* **32**, 1985 (1992).
- [4] M.W. Kissick, E.D. Fredrickson, J.D. Callen *et al.*, *Nucl. Fusion* **34**, 349 (1994).
- [5] K.W. Gentle, R.V. Bravenec, G. Cima *et al.*, *Phys. Plasmas* **2**, 2292 (1995).
- [6] U. Stroth, L. Giannone, H.-J. Hartfuss *et al.*, *Plasma Phys. Control. Fusion* **38**, 1087 (1996).
- [7] J.D. Callen and M.W. Kissick, *Plasma Phys. Control. Fusion* **39**, B173 (1997).
- [8] N. Tamura, S. Inagaki, K. Ida *et al.*, *Phys. Plasmas* **12**, 110705 (2005).
- [9] V.D. Pustovitoy, *Plasma Phys. Control. Fusion* **54**, 124036 (2012).
- [10] T. Iwasaki, S.-I. Itoh, M. Yagi *et al.*, *J. Phys. Soc. Jpn.* **68**, 478 (1999).
- [11] G. Dif-Pradalier, P.H. Diamond, V. Grandgirard *et al.*, *Phys. Rev. E* **82**, 025401 (2010).
- [12] X. Garbet and R.E. Waltz, *Phys. Plasmas* **5**, 2836 (1998).
- [13] P.A. Politzer, *Phys. Rev. Lett.* **84**, 1192 (2000).
- [14] S. Inagaki, T. Tokuzawa, K. Itoh *et al.*, *Phys. Rev. Lett.* **107**, 115001 (2011).
- [15] M. Yagi, A. Matsuyama, N. Miyato and T. Takizuka, 14th International Workshop on Plasma Edge Theory in Fusion Devices (Cracow Poland, 23-25 Sep. 2013).
- [16] N. Miyato, Y. Kishimoto and J. Li, *Phys. Plasmas* **11**, 5557 (2004).
- [17] K. Itoh, K. Hallatschek and S.-I. Itoh, *Plasma Phys. Control. Fusion* **47**, 451 (2005).
- [18] R.D. Hazeltine and J.D. Meiss, *Phys. Rep.* **21**, 1 (1985).
- [19] M. Yagi, S. Yoshida, S.-I. Itoh *et al.*, *Nucl. Fusion* **45**, 900 (2005).